Hindawi Publishing Corporation
Journal of Nanomaterials
Volume 2014, Article ID 214510, 17 pages
http://dx.doi.org/10.1155/2014/214510

Research Article

Size, Temperature, and Strain-Rate Dependence on Tensile Mechanical Behaviors of Ni_3Sn_4 Intermetallic Compound Using Molecular Dynamics Simulation

Hsien-Chie Cheng,[1] Ching-Feng Yu,[2] and Wen-Hwa Chen[2]

[1] *Department of Aerospace and Systems Engineering, Feng Chia University, Taichung 40724, Taiwan*
[2] *Department of Power Mechanical Engineering, National Tsing Hua University, Hsinchu 30013, Taiwan*

Correspondence should be addressed to Hsien-Chie Cheng; hccheng@fcu.edu.tw and Wen-Hwa Chen; whchen@pme.nthu.edu.tw

Received 17 March 2014; Accepted 7 June 2014; Published 27 August 2014

Academic Editor: Fathallah Karimzadeh

This study focuses on exploring the mechanical properties and nonlinear stress-strain behaviors of monoclinic Ni_3Sn_4 single crystals under uniaxial tensile test and also their size, temperature, and strain-rate dependence through constant temperature molecular dynamics (MD) simulation using Berendsen thermostat. The deformation evolution of the Ni_3Sn_4 atomic nanostructure during the tensile test is observed. In addition, the tensile yield strains of various Ni_3Sn_4single crystals at different strain rates and temperatures are characterized through unloading process. At last, by way of linear regression analysis, the corresponding normal elastic stiffness constants are approximated and then compared with the literature theoretical data. The radial distribution function analysis shows that Ni_3Sn_4 single crystal in a one-dimensional nanowire configuration would become a highly disordered structure after thermal equilibration, thereby possessing amorphous-like mechanical behaviors and properties. The initial elastic deformation of Ni_3Sn_4 single crystal is governed by the reconfiguration of surface atoms, and its deformation evolution after further uniaxial tensile straining is characterized by Ni=Sn bond straightening, bond breakage, inner atomic distortion, cross-section shrinking, and rupture. The calculated normal elastic constants of Ni_3Sn_4 single crystal are found to be consistent with the literature theoretical data.

1. Introduction

Green electronic products, especially in lead (Pb-) free and halogen-free manufactures, are extremely popular nowadays due to more and more environmental awareness by consumers and governmental regulations. They have become the main developing trend in the microelectronics community. Various eco- and environmentally-friendly Pb-free substitute solder alloys or compositions, such as Sn-rich alloys including Sn-Ag, Sn-Zn, and Sn-Ag-Cu [1–3], have been proposed in response to the environmental challenges and needs. Despite the fact that Pb-free solders have been proved to be technologically feasible and shown some very promising advantages, many significant technical issues remain to be dealt with before their wide and successful implementation and application. For instance, a Ni layer is typically used in solder interconnects to prevent the Cu metal in the under bump metallurgy (UBM) from chemical reaction with the Sn metal in the Sn2.5Ag solder to form some hard and brittle Cu-Sn intermetallic compounds (IMCs), such as Cu_3Sn [4] and Cu_6Sn_5 [5]. Instead, a Ni_3Sn_4 [6] IMC layer will be formed at the interface between the Ni layer and the Sn metal (shown in Figure 1 [7]). It was reported by Chan et al. [8] that an appropriate IMC layer with a few micrometer thicknesses can upgrade metallurgical bonding strength probably because of its hard properties. Nevertheless, Yao and Shang [9] indicated that as the thickness of the IMC layer increases up to a certain level, the shear strength of the microsolder joints would be greatly downgraded owing to its brittle characteristic, which might eventually cause brittle fracture failure in the microsolder joints when subjected to impact loading. Kim et al. [10] also demonstrated that there is an inverse relation

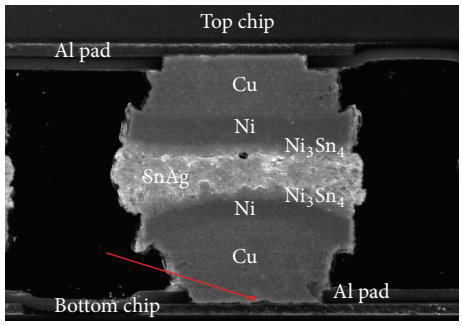

Figure 1: An SEM image of a microsolder joint.

between IMC thickness and solder joint reliability. The risk of brittle fracture in solder interconnects would be increased due to high local stress resulting from extreme thermal-mechanical loading during fabrication process, assembly and environmental testing together with the low surface energy of IMCs. The issue becomes more pronounced for next-generation microelectronic packaging technology, such as three-dimensional (3D) chip stacking packaging, where the dimension of solder interconnects is reduced down to 10~15 μm, and even less than 5 μm in future [11–13]. And at or below this length scale, the thickness of the IMC layer can be as small as one to several grains or as large as up to one half of the height of the solder interconnects (e.g., full IMC solder joints). For better grasp of the thermal-mechanical reliability of the solder interconnects, clear comprehension of their mechanical properties and also their strain, strain rate, size, and temperature dependence is critically crucial.

The material behaviors and properties may vary significantly for IMCs with a thickness ranging from tens of nanometers to tens of micrometers, which are thus difficult or even unable to be precisely and accurately characterized through classical elastic-plastic constitutive models. For micro-/nanomaterial characterization, it is now possible to apply advanced nanoscale testing techniques, such as nanoindentation experiment [14, 15], and atomic modeling methods [16–36], such as molecular dynamics (MD) simulation. However, even with the most advanced testing techniques, precisely characterizing the mechanical and thermodynamic properties of nanoscale IMCs remains great difficulty and challenge, not to mention their strain, strain rate, size, and temperature dependences, due to the inherent limitations of the testing techniques and instruments and also high measurement uncertainty. In addition, experimental testing is typically carried out on a test sample in a bulk polycrystalline form such that single-crystalline material properties of nanomaterials are not readily available.

In recent years, the advance in computer hardware and software has made atomic modeling of nanostructures possible. Atomic modeling can limit the shortage of experimental approaches and also supplement laboratory assessment. Over the past years, various computational approaches have been proposed, including equivalent-continuum modeling (ECM) [20–24], molecular dynamics (MD) simulation [4, 25–31], and quantum mechanics (QM) simulation [19, 32–34]. For example, Cheng et al. [35] and Lee et al. [36] evaluated the elastic properties of Ni_3Sn_4 monocrystal by performing density functional theory (DFT) calculations within the generalized-gradient approximation (GGA) and local density approximation (LDA) using the software CASTEP [37, 38]. However, because of limited computer speed and memory, these studies using first-principles calculations generally adopt an atomic unit cell model with periodic boundary condition to determine the bulk-like properties of a larger system.

This study aims at conducting a comprehensive analysis of the mechanical properties and nonlinear stress-strain behaviors of Ni_3Sn_4 single crystal at room temperature under uniaxial tensile test, and their size, temperature, and strain-rate effects. The alternative focus is placed on the deformation evolution characteristics of the Ni_3Sn_4 atomic nanostructure during uniaxial tensile test. To the author's best knowledge, the present comprehensive analysis is the first to address the issue. The single-crystalline Ni_3Sn_4 systems under investigation are in a one-dimensional (1D) nanowire form. The nanowires are constructed by assembling a number of Ni_3Sn_4 unit cells along the three axes of a prescribed coordinate system. To achieve the goal, an atomic-scale theoretical analysis based on MD simulation is performed. In the MD model, the physical interaction between atoms is simulated by the universal force field [39, 40]. By the proposed tensile MD simulation, the constitutive relationships between stress and strain for Ni_3Sn_4 single crystal are characterized as a function of strain rate. Furthermore, the strain-rate-dependent mechanical properties are examined, including the normal elastic constants, yield strain and strength, ultimate tensile strength, and fracture strain. To demonstrate the effectiveness of the proposed MD model, the calculated normal elastic constants are compared against the literature theoretical results obtained from first-principles calculations.

2. Potential Function of Ni_3Sn_4

In the present MD model, the universal force field (UFF) is applied to simulate the bonding forces between atoms, where bond stretching is described by a harmonic term, angle bending by a three-term Fourier cosine expansion, and torsion and inversion by cosine-Fourier expansion terms. In addition, the Lennard-Jones (LJ) potential is used to describe the van der Waals interactions. Basically, UFF is an all-atom method containing parameters for every atom. The potential energy is expressed as sum of bonded interactions and nonbonded interactions [39, 40]:

$$E_{\text{pot}} = \sum_{b} \left\{ \frac{K_{b0}}{2} (b - b_0)^2 \right\} + \sum_{\theta} \left\{ \frac{K_{\theta 0}}{2} \left(\frac{[\cos\theta - \cos\theta_0]^2}{[\sin\theta_0]^2} \right) \right\} + \sum_{\phi} \left\{ \frac{B_j}{2} \left(1 - d_j \cos\left[n_j \phi\right]\right) \right\}$$

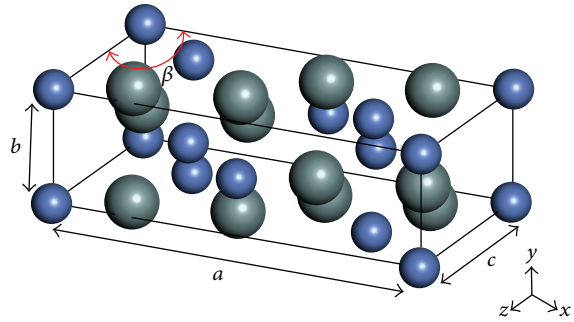

Figure 2: Crystal structure of the Ni_3Sn_4 unit cell (grey spheres represent Ni atoms and purple spheres denote Sn atoms).

$$+\sum_{\omega}\frac{K_{\omega 0}}{2\sin^2(\omega_0)}(\cos\omega-\cos\omega_0)^2$$
$$+\sum_{R}D_0\left[\left(\frac{R_0}{R}\right)^{12}-2\left(\frac{R_0}{R}\right)^{6}\right]+332.0647\sum_{i>j}\frac{q_iq_j}{\varepsilon R}, \quad (1)$$

the first four terms of (1) are the energies associated with bond (b), angle (θ), torsion (ϕ), and out-of-plane (ω) internal coordinates; the last terms are the LJ 12–6 potential and Coulombic potential, denoting the van der Waals interaction and electrostatic energy, respectively. In (1), K_{b0}, $K_{\theta 0}$, and $K_{\omega 0}$ stand for force constant, b_0, θ_0, and ω_0 are equilibrium bond distance and angle, B_j represents tensional barrier, d_j is phase factor, n_j is periodicity, D_0 is equilibrium well depth, R_0 is equilibrium, and ε is relative dielectric constant. In general, the empirical force field parameters in the UFF are derived from quantum modeling.

3. Details of Molecular Dynamics (MD) Simulation

The atomic structure of Ni_3Sn_4 single crystal was comprehensively clarified by Rappé et al. [41], where it is a monoclinic lattice structure, as displayed in Figure 2. The unit cell of Ni_3Sn_4 single crystal is composed of six Ni atoms and eight Sn atoms; the smaller spheres in the lattice represent the Ni atoms and the larger ones the Sn atoms. The unit lattice cell is parallelepiped and consists of dimensions 12.214 Å, 4.060 Å, and 5.219 Å along the three lattice directions (a, b, and c, shown in Figure 2), respectively. There is a nonright angle (β) observed between the lattice vectors a and c. The nonright angle is around 105°, suggesting a nonparallelism between the lattice vector a and the axis x of the predefined rectangular coordinate system. In other words, the axis b is in line with the lattice direction y; and the axis c the lattice direction z. Three different Ni_3Sn_4 nanowire models, as shown in Figure 3, are developed for tensile MD simulation, which are tailored from a single-crystalline Ni_3Sn_4 substrate along the three axes of the predefined rectangular coordinate system, that is, x, y, and z, rather than the crystallographic directions, that is, a, b, and c. During the uniaxial tensile test, the Ni_3Sn_4 nanowires are subjected to tensile strain at a prescribed strain rate along the x, y, and z axes, respectively. Figure 3(a) presents a schematic of the atomic model of the nanowire with the longitudinal dimension along the x-axis. It is evident that the x axis of the predefined coordinate system is not parallel to the lattice vector a. Unlike the nanowire model in Figure 3(a), the longitudinal axis of the other two nanowire atomic models (i.e., Figures 3(b) and 3(c)), which is along the y and z axis, is parallel to the corresponding lattice directions b and c, respectively. It should be noted that the Ni_3Sn_4 nanowires consist of a circular cross section mainly because they would possess the most stable and natural cross-sectional configuration [42–44]. Under the same length of 100 Å, three different nanowire diameters, namely, 14 Å (14ϕ), 18 Å (18ϕ), and 22 Å (22ϕ), are considered in the tensile MD simulation, in which they are labeled with "14$\phi\times$100," "18$\phi\times$100," and "22$\phi\times$100," respectively. Figure 4 shows the atomic models for these Ni_3Sn_4 nanowires.

By using the proposed MD simulation, the stress-strain relations of the 1D nanocrystal structures are simulated by displacing the atoms (the red zone shown in Figure 4) on the top side of the nanowires while fixing those of the bottom (the orange zone shown in Figure 4) at a constant strain rate $\dot{\varepsilon}$. To assess the strain-rate effects, the Ni_3Sn_4 nanowires are loaded at five different strain rates, namely, 10^{-4}% ps^{-1}, 5×10^{-4}% ps^{-1}, 10^{-3}% ps^{-1}, 5×10^{-3}% ps^{-1}, and 10^{-2}% ps^{-1}. Furthermore, to investigate the influences of temperature on the stress-strain relations of the Ni_3Sn_4 nanowires, Berendsen thermostat [45] is applied for constant temperature MD simulation at three different temperatures, that is, 300 K, 500 K, and 700 K. These temperatures are well below the melting point of Ni_3Sn_4 crystal (i.e., 1096 K) [46], thereby ensuring that Ni_3Sn_4 nanocrystal during the uniaxial tensile test remains in solid phase.

In the MD simulation, a total of 5×10^3 simulation time steps (N_{step}) with a time step size (Δt) of 1×10^{-3} ps are first employed for simulating the initial equilibrated unstrained configuration. After the equilibration, a time step size of 1×10^{-3} ps is also carried out for each incremental strain during the uniaxial tensile test. By varying the total number of time steps from 10^3 to 10^5, five different strain rates, defined below, in the range of 10^{-4}% ps^{-1} to 10^{-2}% ps^{-1} can be achieved and simulated:

$$\dot{\varepsilon}=\frac{\Delta\varepsilon}{N_{\text{step}}\Delta t}. \quad (2)$$

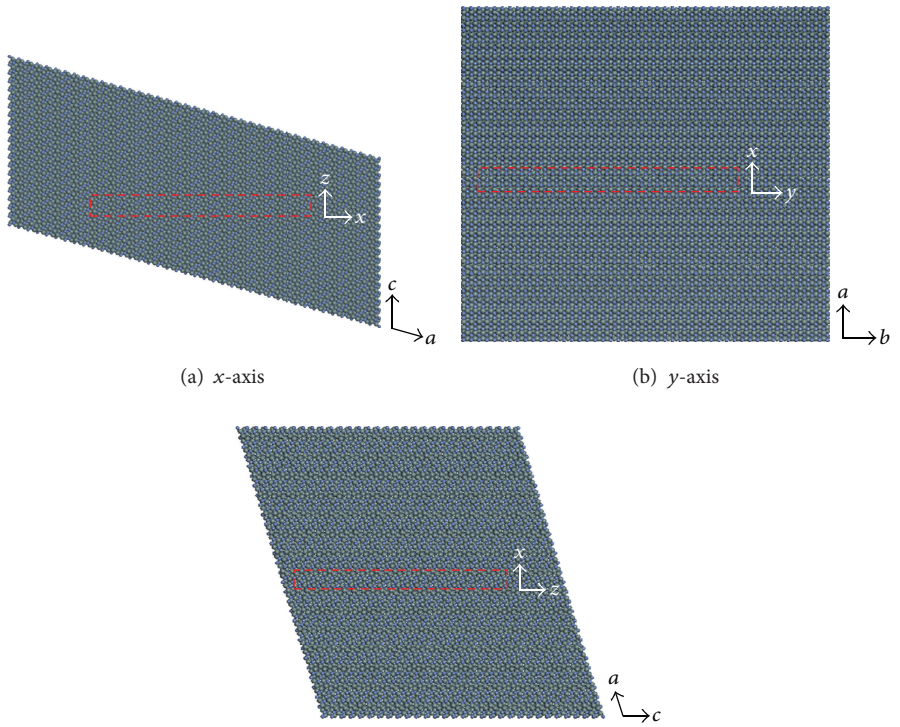

(a) x-axis (b) y-axis

(c) z-axis

FIGURE 3: Schematic of three different Ni_3Sn_4 nanowire models tailored from a single-crystalline Ni_3Sn_4 substrate along the three axes of the predefined rectangular coordinate system.

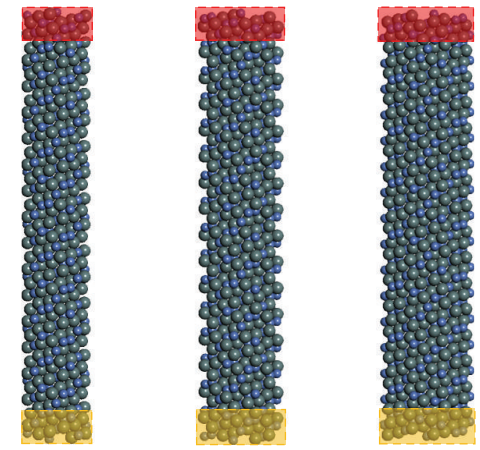

$14\phi \times 100$ Å $18\phi \times 100$ Å $22\phi \times 100$ Å

FIGURE 4: Atomic structures of the three Ni_3Sn_4 nanowire models of three different sizes.

The stress on a nanostructure is calculated by the following equation [47]:

$$\sigma(\varepsilon) = \frac{1}{N\Omega^i} \sum_{i=1}^{N} \sum_{\substack{j=1 \\ j \neq i}}^{N} F_{ij}(\varepsilon)\, r_{ij}(\varepsilon), \tag{3}$$

where N is the total number of atoms, Ω^i denotes the volume of atom i, F_{ij} represents the pairwise interatomic force between atoms i and j, and r_{ij} is the interatomic distance between atoms i and j.

4. Results and Discussion

Figures 5 and 6 reveal the equilibrated atomic structures of the three Ni_3Sn_4 nanowire models and their corresponding radial distribution function (RDF) value after thermal equilibration. The RDF analysis is a key way to disclose the structure features of a nanosystem, particularly for liquids and amorphous structures. The RDF can be calculated as

$$g(r) = \frac{V}{N^2} \left\langle \sum_{i=1}^{n} \frac{n(r)}{4\pi r^2 \Delta r} \right\rangle, \tag{4}$$

where V represents the volume of the system and $n(r)$ the number of particles, which can be found in the shell from r to $r + \Delta r$. In the study, for the binary intermetallic compounds system, the RDF for atom α and atom β is derived by

$$g(r) = \frac{V}{N_\alpha N_\beta} \left\langle \sum_{i=1}^{N_\alpha} \frac{n_{i\beta}(r)}{4\pi r^2 \Delta r} \right\rangle. \tag{5}$$

According to the calculated results, it is found that the Ni_3Sn_4 nanowires transform homogenously from a crystalline to

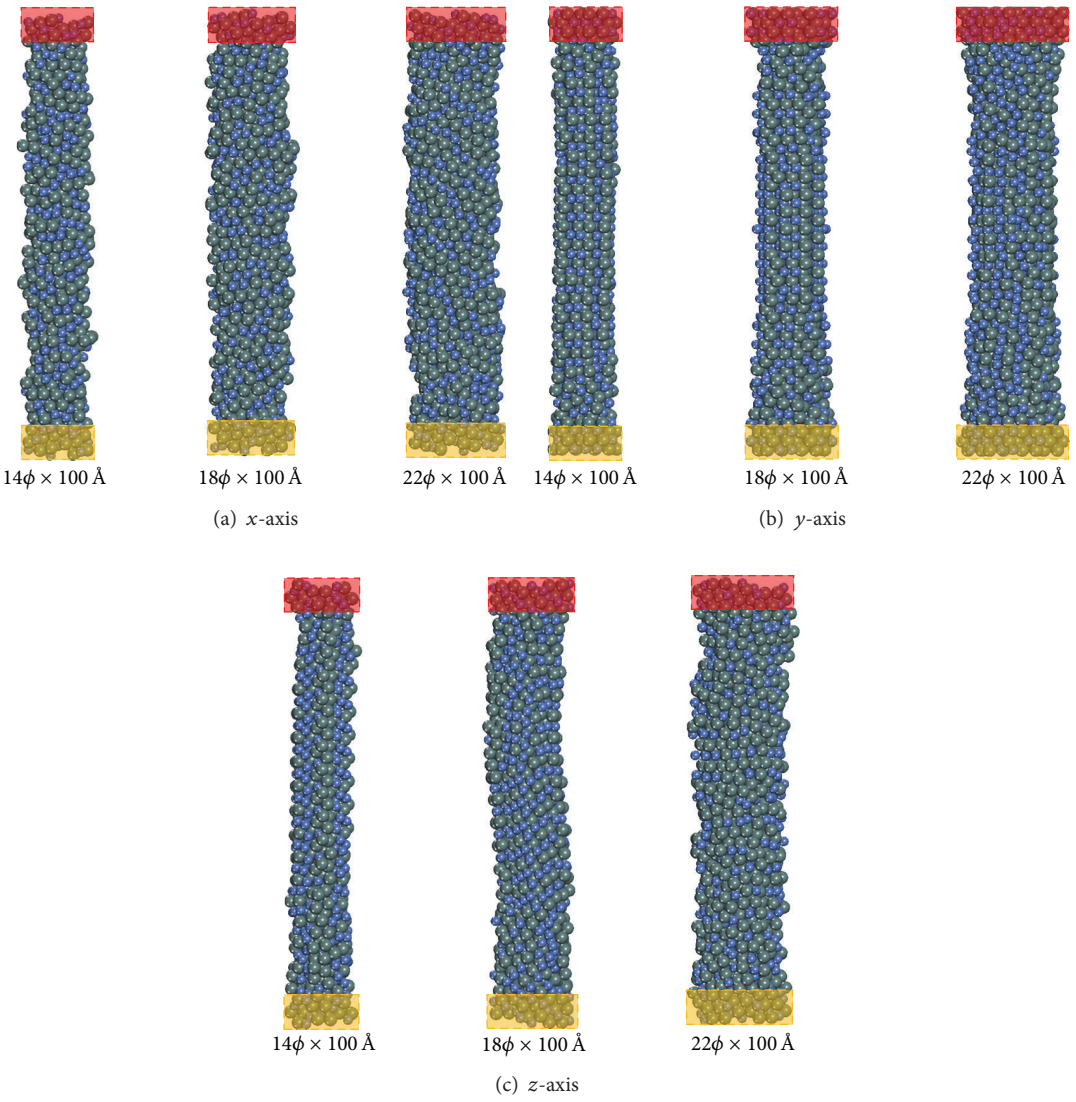

FIGURE 5: Equilibrated atomic structures of the three Ni_3Sn_4 nanowire models of three different sizes.

amorphous-like state after thermal equilibration. It is also noted that the RDF would considerably decrease with the increase of the diameter, suggesting that the degree of amorphization is reduced with an increasing cross-sectional area. This observation is generally applicable for various materials, such as metals, semiconductors, and ceramics [48–50].

The stress-strain responses of the Ni_3Sn_4 nanowires, starting from an initial unstressed state to a complete rupture state, are exhibited in Figures 7(a)–7(c). Figure 8 further presents the strain-rate effects on the stress-strain response of the Ni_3Sn_4 nanowire with the longitudinal dimension along the x-axis. According to Figures 7 and 8, the strength of the single-crystalline Ni_3Sn_4 nanostrctures (i.e., "14ϕ × 100," "18ϕ × 100," and "22ϕ × 100") would all substantially decrease with an increasing temperature. This could be ascribed to the fact that the increase of temperature tends to weaken the interatomic bonds between Ni and Sn atoms, thereby resulting in reduced strength. Apart from that, as indicated in Figure 8, for all the simulation temperatures and nanowire sizes (diameters), the strength would also increase as the strain rate increases. The strain-rate effect can be elucidated by means of the structural disorder in the Ni_3Sn_4 nanowires due to external loading [48, 49]. In general, a higher strain rate could enhance the degree of structural disorder of the nanostructure, thereby increasing the extent of amorphization [48–50]. For an amorphization system, the disordered nature does not allow the formation of well-defined slip planes. Because of the absence of the dislocation planes, no abrupt transformation of the system during deformation can be detected. Consequently, the strength would be significantly increased as the strain rate increases [48–50]. Finally, the results in Figures 7 and 8 also demonstrate that the strength of the Ni_3Sn_4 nanowires would rise with the increase of the nanowire diameter. This size effect has also been observed in many literature studies [18, 49, 51]. The significant size effect may be mainly due to the surface effects

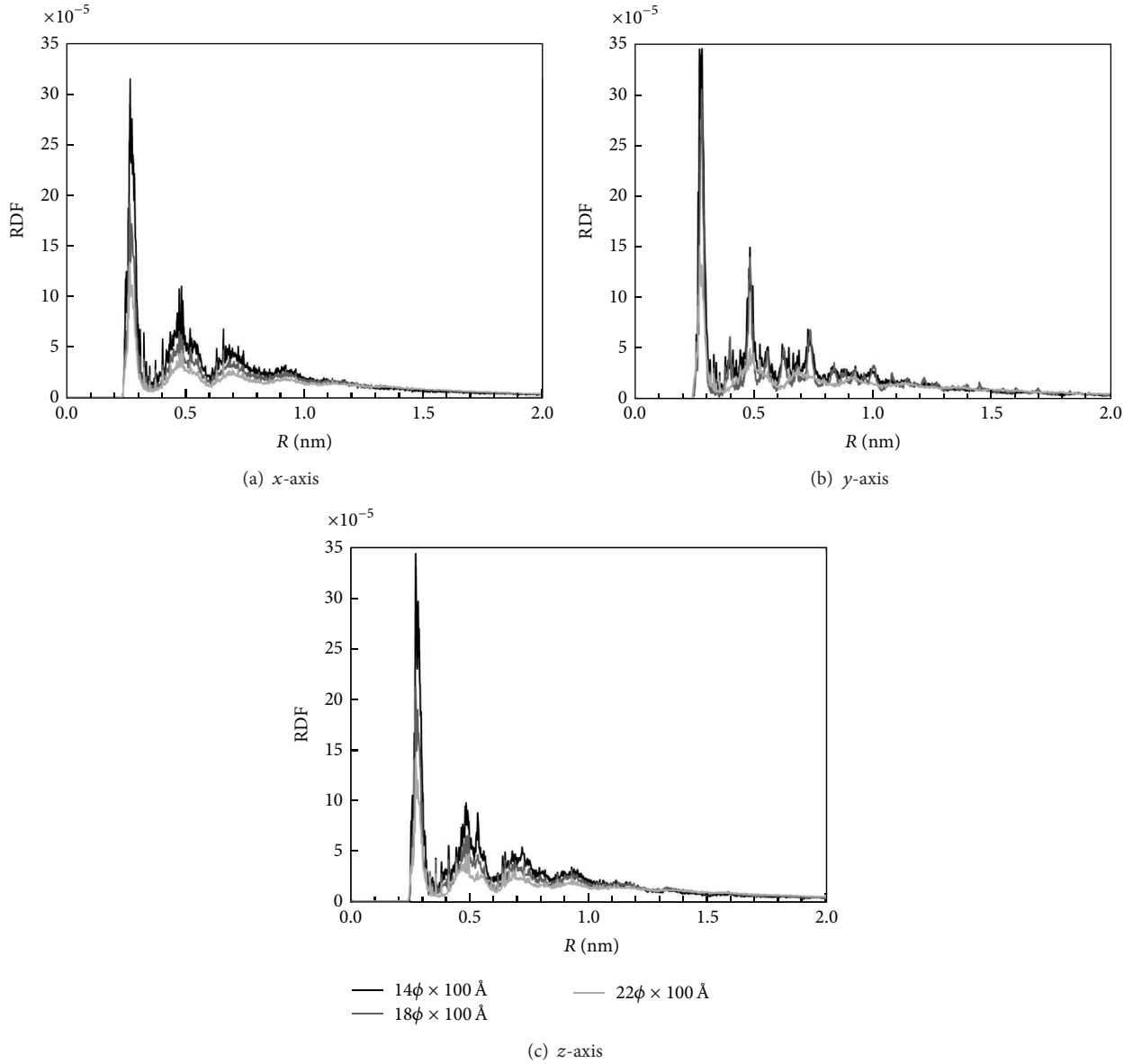

Figure 6: Radial distribution function (RDF) of the three Ni_3Sn_4 nanowire models after thermal equilibration.

of nanocrystals, including surface energy [52], surface stress [53], and surface relaxation [54], and the effects are strongly dependent on the surface to volume ratio. For nanosize particles, wires, and films, the corresponding surface to volume ratios are significant, and so are the surface or boundary effects.

The deformation characteristics of the nanostructure during the stress-strain evolution are demonstrated using the tensile σ_{11}-ε_{11} stress-strain response of the "22ϕ×100" Ni_3Sn_4 nanowire (see Figure 4) at 300 K and strain rate 10^{-4}% ps^{-1}, which is shown in Figure 9. Evidently, the system exhibits a continuous mechanical deformation before fracture. The nanowire initially starts a linearly elastic deformation from its unstrained configuration (i.e., point (1) in Figure 9(a)), where a linear stress-strain relation is given, or in other words, the stress is linearly proportional to the applied strain. This relation follows closely the well-known Hooke's law, and the slope is known as the elastic modulus of Ni_3Sn_4 single crystal in the x-axis. Furthermore, after a critical threshold value of the stress, referred as the proportional limit (i.e., "σ_{pl}" in Figure 9(a)), the nanocrystal structure experiences extraordinarily large nonlinearly elastic deformation. After the critical threshold stress value, the deformation is followed by a nonlinear plastic deformation, causing a permanent or residual strain after unloading. The threshold stress value that transits from nonlinear elasticity to plasticity is referred as the yield stress or yield strength σ_y (i.e., point (2) in Figure 9(a)), and the corresponding strain is known as the yield strain ε_y. To determine the yield strain, unloading process is carried out at the several different applied strains and the associated residual strains are characterized in Figure 9(c). It is evident to see that no residual strain is observed as the applied strain

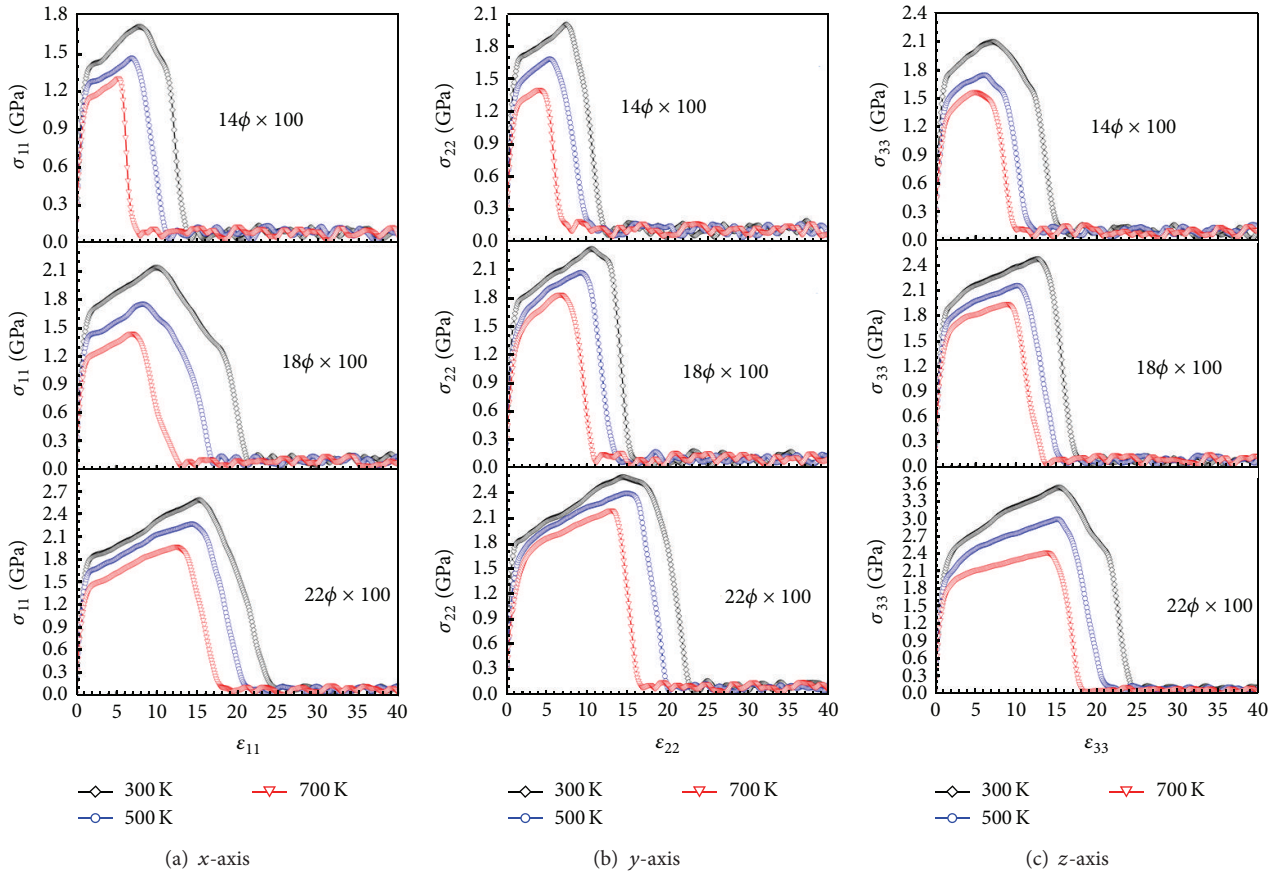

FIGURE 7: Stress-strain responses of the three Ni_3Sn_4 nanowire models of three different sizes at 300 K, 500 K, and 700 K and the strain rate of 10^{-4}% ps^{-1}.

is below 3.0%, indicating that the tensile yield strain in the x-axis is around 3.0%, and from Figure 9(a), the corresponding tensile yield strength is about 2.01 GPa. Subsequently, the stress increases with an increasing strain until a maximum stress level is reached. The maximum stress is well known as the ultimate tensile stress or ultimate tensile strength σ_u, and the corresponding strain is referred to as the ultimate tensile strain ε_u. For the Ni_3Sn_4 nanowire under the σ_{11}-ε_{11} tensile test, the ultimate tensile strain of Ni_3Sn_4 nanowire with the longitudinal dimension parallel to the x-axis is around 14.5%, and the ultimate tensile strength is about 2.67 GPa. Furthermore, beyond the maximum stress (point "3" in Figure 9(a)), the stress starts to gradually decrease despite an increasing strain. This is mainly ascribed to a homogenous deformation as a result of the absence of dislocation planes. The phenomenon is well known as necking. The ultimate tensile strain is the onset point of the necking process. A snapshot of the onset point of the necking phenomenon (i.e., point (3) in Figure 9(a)) is exhibited in Figure 9(b)-(3). Beyond the point, the necking process continues, further decreasing the cross-sectional area of the neck, as can be seen in Figure 9(b)-(4) corresponding to the point (4) in Figure 9(a) (i.e., ε_{11} = 23.0%), and in Figure 9(b)-(5) corresponding to the point (5) in Figure 9(a) (i.e., ε_{11} = 25.0%). The Ni_3Sn_4 nanowire becomes fully ruptured at a strain of ε_{11} = 31.0%. Accordingly, the fracture strain ε_f is 31.0%.

To have a better insight into the mechanism behind the stress-strain behavior, the atomic rearrangement of the nanowire structure during the deformation evolution process is characterized. Figure 10 displays a small section of the [0 0 1] crystalline plane of the "$22\phi \times 100$" Ni_3Sn_4 nanowire model with the longitudinal dimension parallel to the x-axis shown in Figure 4, and the section is also indicated in Figure 9(b)-(1). The left side of the section is the free surface of the nanowire, and the right side is toward the centerline (i.e., the central longitudinal axis) of the nanowire. The atoms within the dash box are monitored during the deformation evolution process to highlight the atomic rearrangements. In addition, the Sn atoms in the section are, respectively, labeled from 1 to 9 (i.e., Sn-1~Sn-9), and the Ni atoms from 1 to 6 (i.e., Ni-1~Ni-6), as indicated in Figure 11. Noticeably, four specific stages of atomic arrangements during the deformation evolution process are detected, namely, initial equilibration, yielding, ultimate tensile strength, and necking deformation. Figure 11(a) shows the initial equilibrated nanowire prior to stretching. It is found that the surface atoms (i.e., Sn-1, Sn-2, and Ni-1) form a noticeable relaxed surface configuration due to the free surface condition while the inner atoms

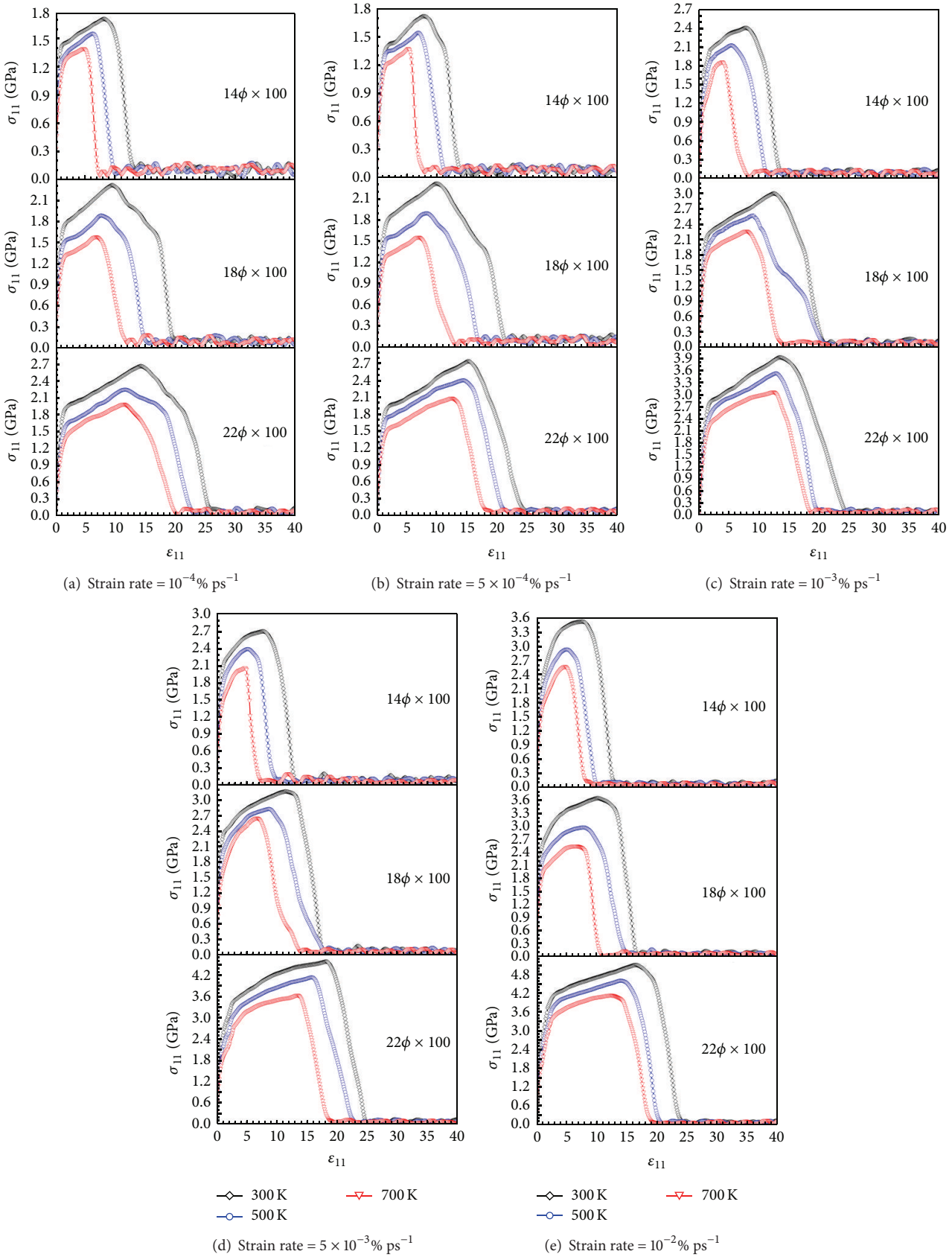

(a) Strain rate = 10^{-4}% ps^{-1} (b) Strain rate = 5×10^{-4}% ps^{-1} (c) Strain rate = 10^{-3}% ps^{-1}

(d) Strain rate = 5×10^{-3}% ps^{-1} (e) Strain rate = 10^{-2}% ps^{-1}

FIGURE 8: Stress-strain responses of the Ni_3Sn_4 nanowire model of three different sizes constructed along the x-axis as a function of temperature and strain rate.

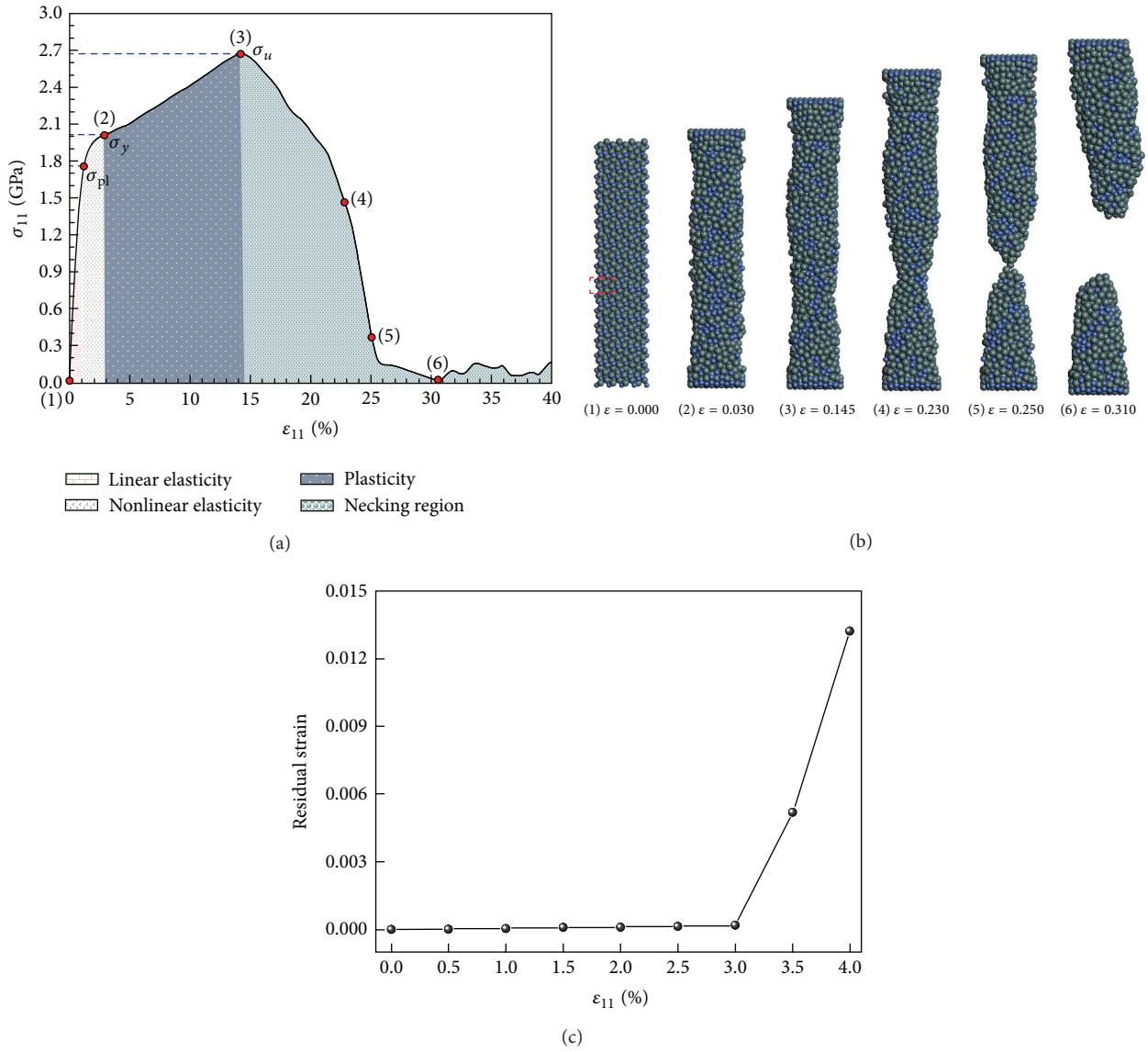

FIGURE 9: (a) The tensile σ_{11}-ε_{11} stress-strain evolution of the "22ϕ × 100" Ni_3Sn_4 nanowire model at 300 K and strain rate = 10^{-4}% ps^{-1}, (b) snapshots of fracture evolution of the Ni_3Sn_4 atomic structure at various strains, and (c) the residual strain after unloading versus the applied strain.

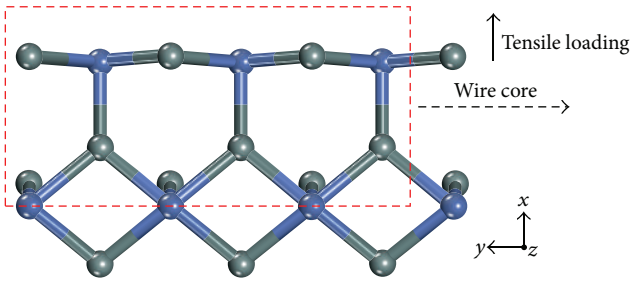

FIGURE 10: Section of [0 0 1] crystalline plane of 22ϕ × 100 Ni_3Sn_4 nanowire constructed along principle axis x.

(i.e., Sn-7, Sn-8, Ni-5, Ni-6, and Sn-9) would maintain their initial state or position. At the beginning of the tensile loading, stretching causes the surface atoms, Sn-1 and Ni-1, to undergo significant separation. By contrast, as can be seen in Figure 11(b), the inner atoms would only have a small elastic deformation. The bond breakage of the Ni-2=Sn-3 bond reveals the commencement of irreversible deformation or strain, which is considered as the onset of yielding. As the Ni-2 and Sn-3 atoms are further pulled apart, accompanied by the straightening of nanowire, the necking process starts (see Figure 9(b)-(3)), in which, as can be seen in Figure 11(c), the bond breakage of the Ni-4=Sn-6 bond takes place. When the loading exceeds the bond strength, the Sn-3=Ni-3 bond is broken and a new surface is created, which can be seen in Figure 11(d). This leads to the contraction of the cross-sectional area of the necked region (Figure 9(b)-(4)). Figure 11(d) also reveals that the Sn-2, Ni-1, and Sn-3 atoms are separated from

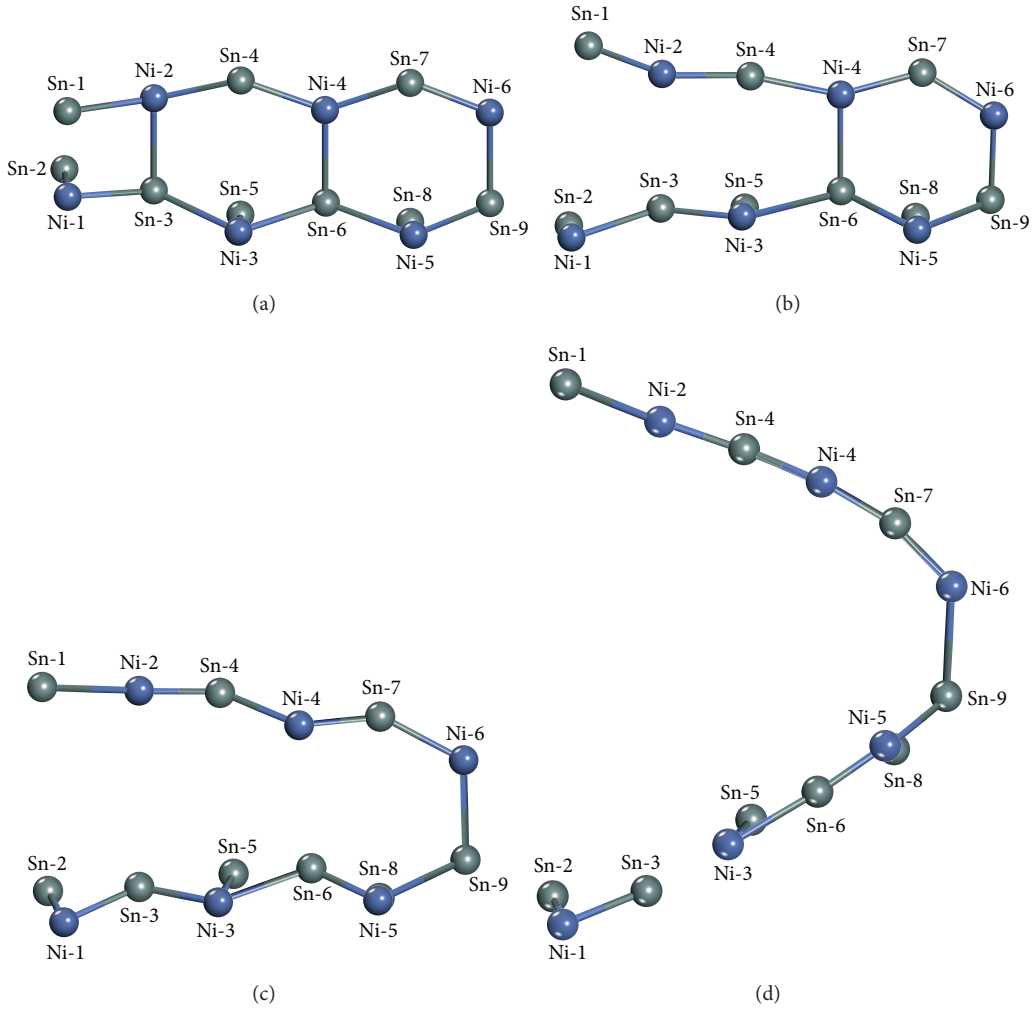

Figure 11: Rearrangement of atoms in the red dash box of Figure 9(b)-(1) under tensile loading at (a) initial equilibration, (b) yielding, (c) ultimate tensile strength, and (d) necking.

the Ni-3 atom. Accordingly, the stretching of the nanowire is characterized by bond straightening, bond breakage, inner atomic distortion, and cross-section shrinking until forming a single-atom neck, and rupture.

To assess the temperature dependence, the σ_{11}-ε_{11} stress-strain behavior at 700 K and the same strain rate as used in Figure 9 (i.e., 10^{-4}% ps^{-1}) is calculated and the result is illustrated in Figure 12. It is noted that the system entropy would increase with an increasing temperature, thereby leading to a much more significant vibration of atoms. The increasing vibration would further result in much larger structure instability, thereby causing atomic structure reconstruction. It can also be observed from Figure 12(b)-(2) that the Ni_3Sn_4 nanowire at a higher temperature is more inclined to undergo an early onset of atomic structure reconstruction, as compared to that at 300 K shown in Figure 9(b)-(2). Consequently, the yield strain of the Ni_3Sn_4 nanowire at 700 K is 50% lower than that at 300 K, and according to Figure 12(a), the corresponding yield strength is 35% less than that at 300 K. In addition, the ultimate tensile strength of the Ni_3Sn_4 nanowire at 700 K occurs at a strain (i.e., ε_{11} = 11.5%, as shown in Figure 12(b)-(3)) much less than that at 300 K (i.e., ε_{11} = 14.5%). Further increasing the strain would create a more excessive necking behavior, as shown in Figures 12(b)-(4) and 12(b)-(5). At last, the nanowire is completely ruptured at ε_{11} = 0.268.

It is worthy of noting that there exhibits a unique phenomenon in the longitudinal section views of the atomic model of the "22ϕ×100" Ni_3Sn_4 nanowireat 300 K and 700 K, as shown in Figure 13. The figure reveals that the Sn atoms tend to be dispelled to the surface of the Ni_3Sn_4 nanowire while the Ni atoms would gather inside as the temperature increases from 300 K to 700 K. This may be due to the fact that Ni atoms would have much larger cohesive energy, as compared to Sn atoms. The hypothesis is confirmed by the literature finding [55], in which the cohesive energy for Ni and Sn atoms is about 4.44 eV/atom and 3.14 eV/atom, respectively.

The σ_{11}-ε_{11} stress-strain response of the Ni_3Sn_4 nanowire model with the longitudinal dimension parallel to the x-axis, as shown in Figure 4, at 300 K and the strain rate of 10^{-2}% ps^{-1} is predicted to examine the effects of strain rate, and

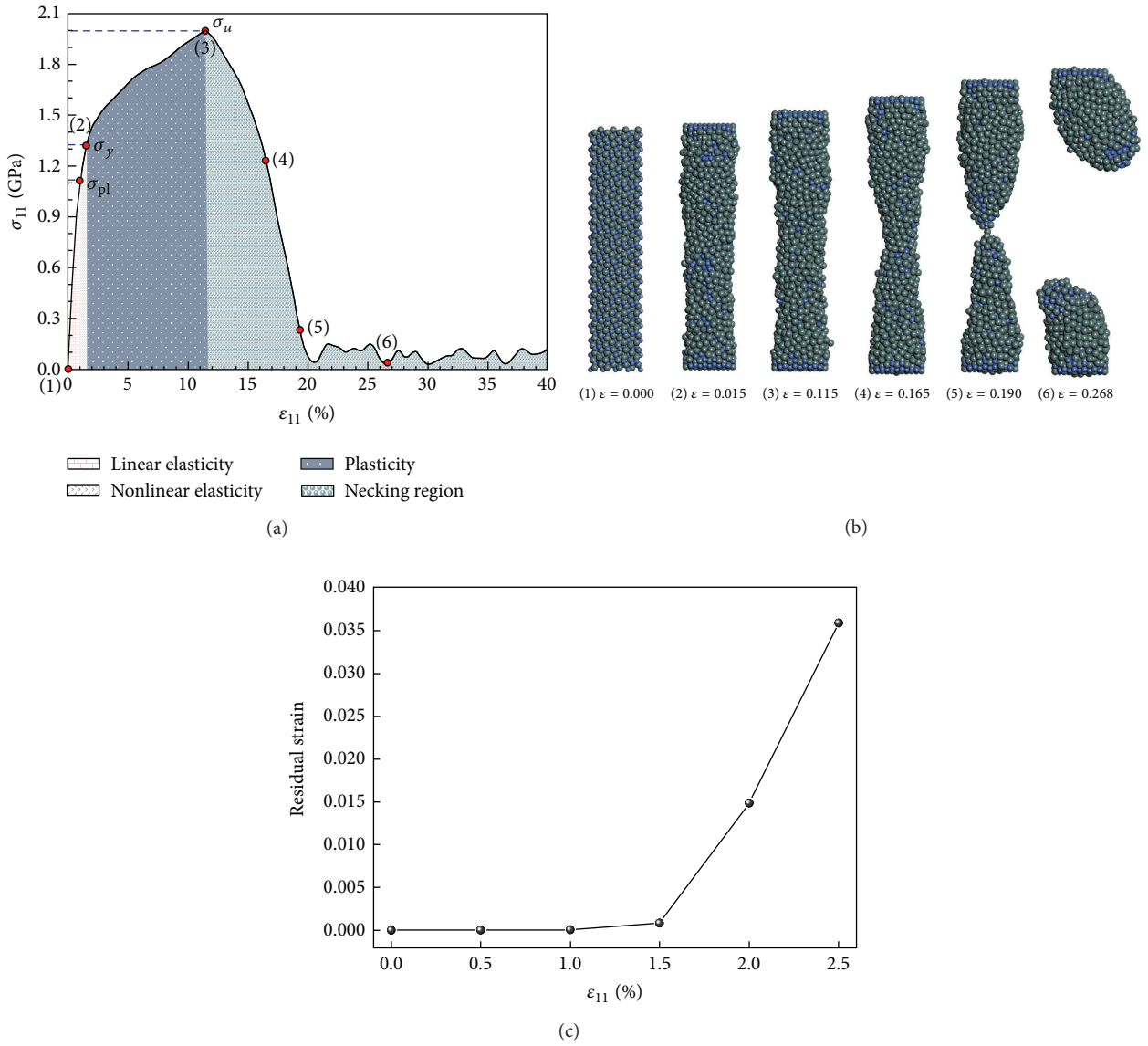

FIGURE 12: (a) The tensile σ_{11}-ε_{11} stress-strain evolution of the "22ϕ × 100" Ni_3Sn_4 nanowire model at 700 K and strain rate = 10^{-4}% ps^{-1}, (b) snapshots of fracture evolution of the Ni_3Sn_4 atomic structure at various strains and (c) the residual strain after unloading versus the applied strain.

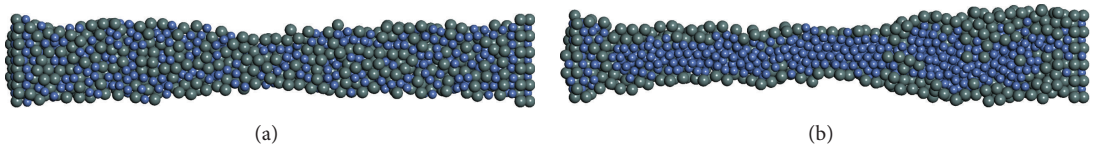

FIGURE 13: Longitudinal section of the "22ϕ × 100" Ni_3Sn_4 nanowire constructed along the x-axis at (a) 300 K and (b) 700 K.

the result is shown in Figure 14. By comparing the result shown in Figure 9 (i.e., at the strain rate of 10^{-4}% ps^{-1} and 300 K), the stress-strain behavior of the Ni_3Sn_4 nanowire is found to be markedly influenced by the applied strain rate. The elastic stiffness would increase with an increasing strain rate, thereby leading to much greater yield strength. Subsequently, the corresponding yield strain is also estimated through unloading process at different applied strains, and the result is given in Figure 14(b). From Figure 14(b), it is found that the yield strain is around 4.5%, and moreover, according to Figure 14(a), the corresponding yield strength is about 4.30 GPa. Comparatively, the yield strength and

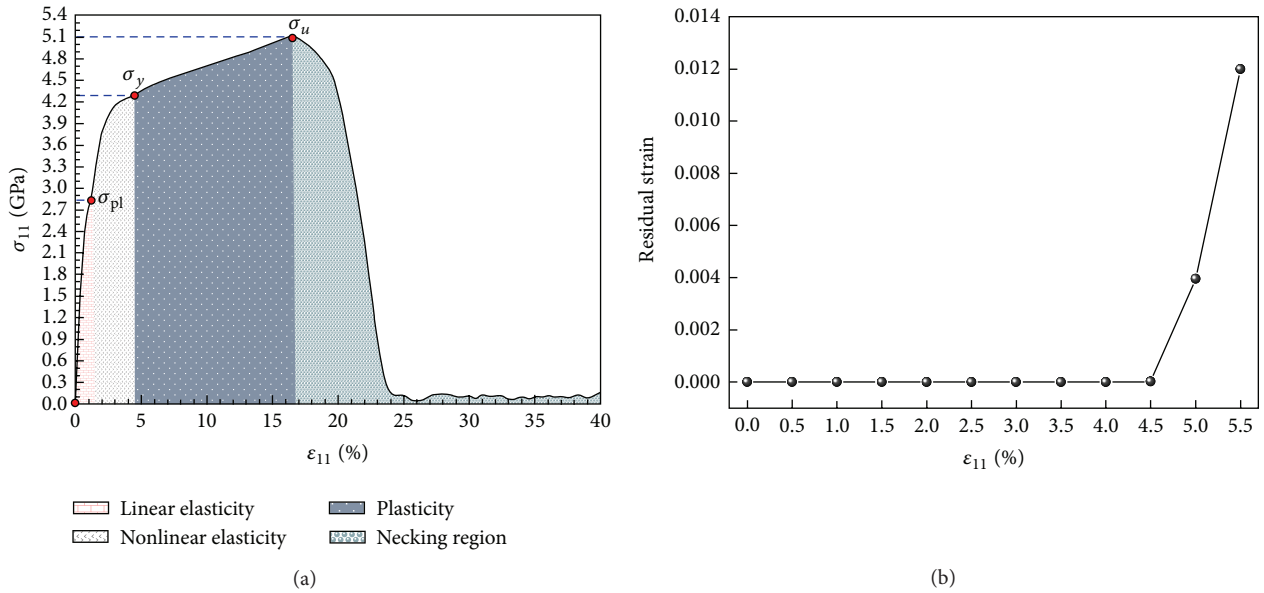

FIGURE 14: (a) The tensile σ_{11}-ε_{11} stress-strain evolution of the "$22\phi \times 100$" Ni_3Sn_4 nanowire model at 300 K and strain rate = 10^{-2}% ps^{-1}, (b) the residual strain after unloading versus the applied strain.

yield strain of the nanowire at the strain rate of 10^{-2}% ps^{-1} are about 114% and 66% higher than those of the low strain rate (10^{-4}% ps^{-1}) shown in Figure 9, respectively. It is also found that the ultimate tensile strength and strain are all raised by 91% and 15% as the strain rate increases from 10^{-4}% ps^{-1} to 10^{-2}% ps^{-1}.

The normal elastic constants of Ni_3Sn_4 single crystal, including C_{11}, C_{22}, and C_{33}, at different strain rates and temperatures are predicted according to the slope of the stress-strain responses before the yield point is reached. To achieve the goal, a linear regression analysis is performed to determine the least squares best fit straight line of the discrete stress-strain data points obtained from the tensile MD simulation, and the slope of the straight lines yields the normal elastic constants. Furthermore, a factor λ, known as the correlation coefficient, is applied to quantify the degree of linearity between the stress-strain data points. In other words, the correlation coefficient measures the degree of linear correlation between stress and strain: in general, the greater the correlation coefficient, the better the least square fit. For instance, $\lambda = 1$ represents the best fit and vice versa.

By the linear regression analysis, the least squares best fit straight lines of the σ_{11}-ε_{11} stress-strain response of the "$22\phi \times 100$" Ni_3Sn_4 nanowire model with the longitudinal dimension parallel to the x-axis, as shown in Figure 4, at five different strain rates and at temperatures 300 K and 700 K are shown in Figures 15 and 16. The associated correlation coefficients λ are also shown in the figures, which are roughly in the range of 94–99%, suggesting that there is a significant linear correlation between stress and strain. The results also show that an increasing strain rate would stiffen the elastic properties of the nanocrystal and so upgrade the normal elastic constant C_{11}, probably because of the change in deformation mechanism. The material stiffening behavior has been observed in numerous previous studies on a number of metals (see, e.g., [56–58]). Table 1 further demonstrates the predicted normal elastic constants, namely, C_{11}, C_{22}, and C_{33}, as a function of the nanowire diameter, strain rate, and temperature by carrying out the tensile stress-strain tests on the three Ni_3Sn_4 nanowire models, shown in Figure 4, with the longitudinal dimension parallel to the x-, y-, and z-axis, respectively. Likewise, it is clear to see that the normal elastic constants are likely to be totally independent of the strain rate as the strain rate is below 5×10^{-4}% ps^{-1}. Accordingly, the strain rate (5×10^{-4}% ps^{-1}) can be considered as the threshold value of the strain-rate dependence of the normal elastic constants of the Ni_3Sn_4 nanowire, and the strain rates below which can be all treated as a quasistatic strain rate. Moreover, according to Table 1, the normal elastic constants of the Ni_3Sn_4 nanowires would increase with an increasing nanowire diameter while considerably decreasing with an increasing temperature. The calculated normal elastic constants are further compared with the published theoretical data [35, 36]. There is a good agreement that can be found between present results and the published theoretical data. For example, Cheng et al. [35] performed the density functional theory calculations to predict the normal elastic constants of Ni_3Sn_4 IMC. Their results showed that the normal elastic constants C_{11}, C_{22}, and C_{33} of the Ni_3Sn_4 IMC are around 192.2, 176.5, and 204.6 GPa, respectively. In addition, these three normal elastic constants of Ni_3Sn_4 IMC were also assessed by Lee et al. [36] through first-principles calculations. They found that the three normal elastic constants are about 155.0, 155.7, and 180.1 GPa, respectively. By comparing the present calculation results in Table 1 with

Table 1: The normal elastic constants as a function of size, strain rate, and temperature.

		$\dot{\varepsilon} = 10^{-4}\%\ \text{ps}^{-1}$		$\dot{\varepsilon} = 5 \times 10^{-4}\%\ \text{ps}^{-1}$		$\dot{\varepsilon} = 10^{-3}\%\ \text{ps}^{-1}$		$\dot{\varepsilon} = 5 \times 10^{-3}\%\ \text{ps}^{-1}$		$\dot{\varepsilon} = 10^{-2}\%\ \text{ps}^{-1}$	
		300 K	700 K	300 K	700 K	300 K	700 K	300 K	700 K	300 K	700 K
$14\phi \times 100$ Å	C_{11}	134.7	105.8	133.8	106.1	154.8	131.5	193.5	170.1	232.8	214.8
	C_{22}	132.5	102.6	133.4	103.3	153.6	129.6	191.3	169.2	230.1	213.7
	C_{33}	149.2	121.4	150.1	122.1	176.1	152.3	218.5	196.4	252.1	234.8
$18\phi \times 100$ Å	C_{11}	156.1	119.6	156.6	120.1	182.3	160.1	220.3	191.0	244.7	211.5
	C_{22}	152.6	117.2	153.2	118.0	179.5	157.4	215.2	188.6	242.6	209.3
	C_{33}	169.5	139.5	169.8	140.2	201.1	175.6	236.6	209.4	272.5	241.1
$22\phi \times 100$ Å	C_{11}	168.4	125.2	168.9	126.1	193.1	165.5	238.7	205.3	273.7	241.6
	C_{22}	153.7	122.3	154.1	122.5	189.6	164.3	234.1	201.6	268.1	239.4
	C_{33}	176.1	140.6	177.0	140.8	217.1	181.6	255.6	223.1	295.4	261.7

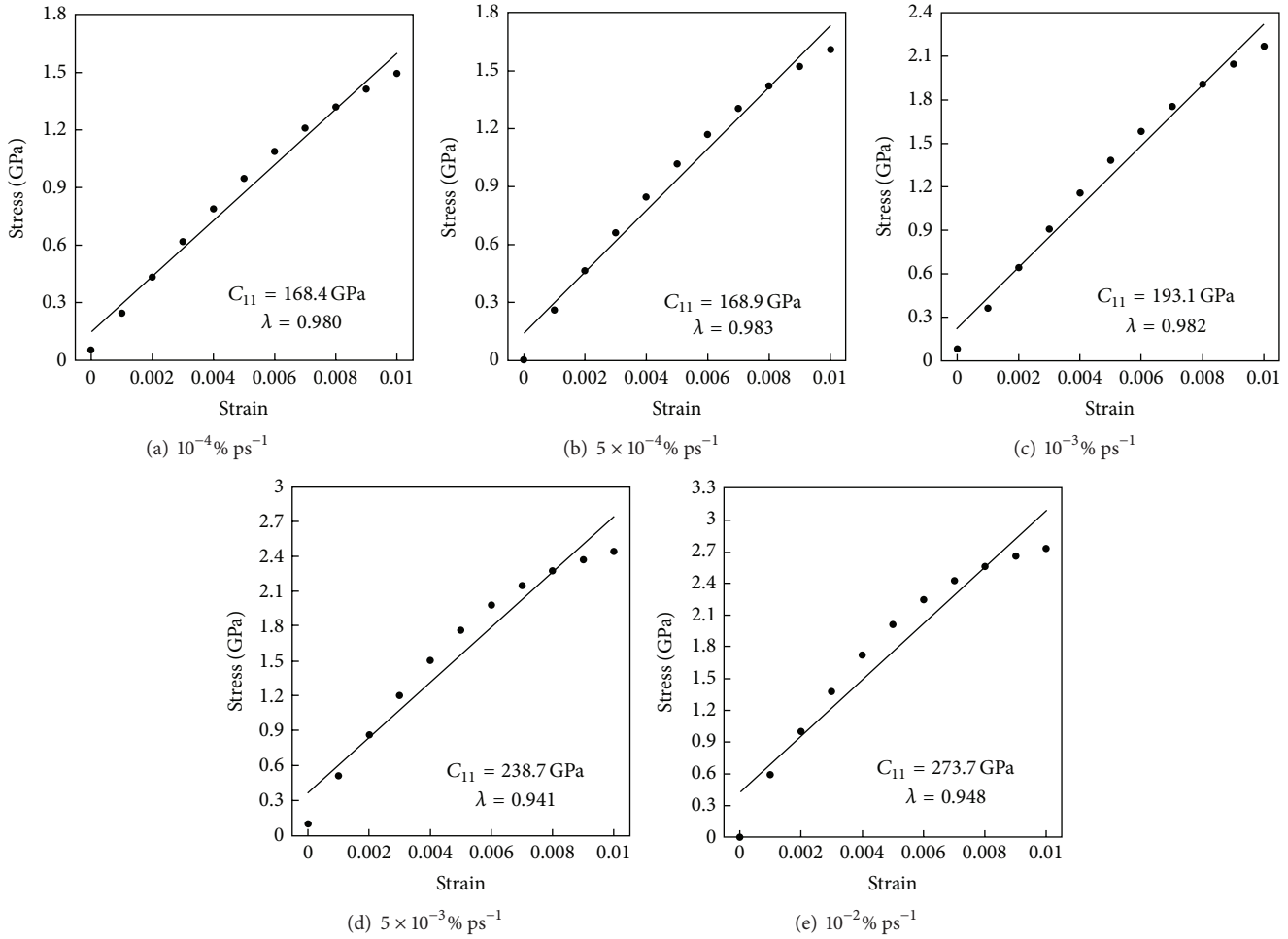

Figure 15: Determination of the C_{11} at 300 K and five different strain rates.

those literature findings, a satisfactory consistency between them is observed. Figure 17 further plots the ultimate tensile strength of the Ni_3Sn_4 nanowire model, shown in Figure 4, of three different sizes as a function of temperature and strain rate. Evidently, the ultimate tensile strength varies substantially with the temperature and applied strain. More specifically, an increasing temperature would reduce it while an increasing strain rate would upgrade it. This could be due to the fact that as the strain rate is below the threshold value, a decreasing strain rate would slightly lessen the normal elastic constants of the nanocrystal.

5. Conclusions

In this study, the mechanical properties and nonlinear stress-strain behaviors of Ni_3Sn_4 single crystals and their size,

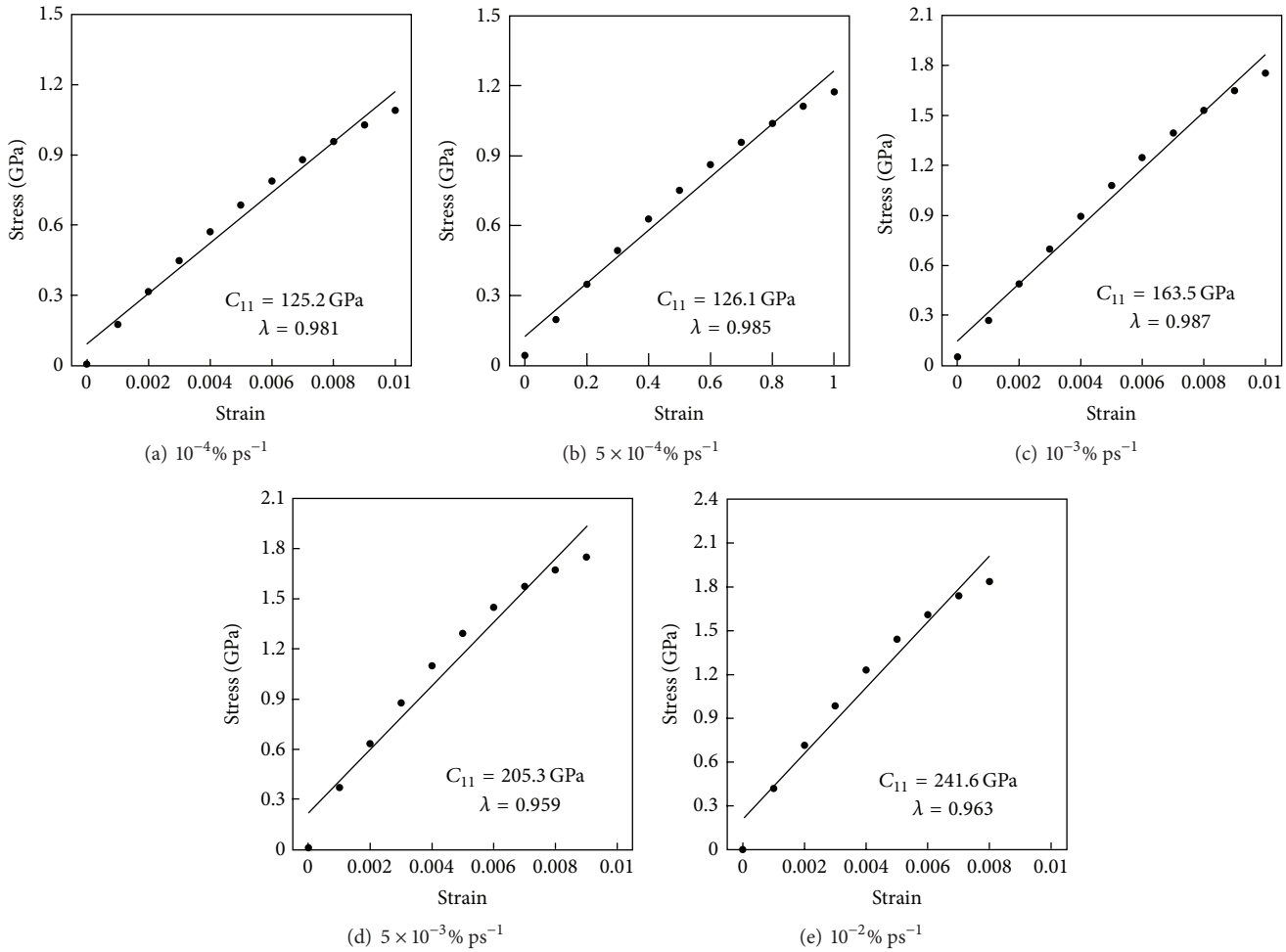

Figure 16: Determination of the C_{11} at 700 K and five different strain rates.

temperature, and strain-rate dependences are extensively addressed through canonical ensemble MD simulation using Berendsen thermostat. The characteristics of the deformation evolution of the Ni_3Sn_4 nanostructure during the tensile test are also addressed according to the stress-strain behavior and atomic rearrangement. Additionally, the tensile yielded strains of Ni_3Sn_4 single crystals at different strain rates and temperatures are characterized through unloading process. Finally, the normal elastic stiffness constants of Ni_3Sn_4 single crystal are characterized through the least squares best fit straight line of the discrete stress-strain data points using linear regression analysis, and most importantly, compared with the literature theoretical findings. It is shown that the present calculations are in good agreement with the literature theoretical data. Some important conclusions are drawn as follows.

(1) From the radial distribution function analysis, it is found that Ni_3Sn_4 single crystal in a one-dimensional nanowire configuration would become a highly disordered structure after thermal equilibration, thereby possessing amorphous-like mechanical behaviors and properties.

(2) The stress-strain behavior of Ni_3Sn_4 single crystal, such as the elastic modulus, yield strength, and strain and ultimate tensile strength and strain, is very sensitive to the nanowire diameter, applied strain rate, and temperature. Specifically, they would increase with an increasing strain rate and nanowire diameter while decreasing with temperature.

(3) From the stress-strain evolution, the Ni_3Sn_4 nanowire under tensile loading would experience linear elasticity, nonlinear elasticity, nonlinear plasticity, necking process, and fracture.

(4) From the fracture evolution of the Ni_3Sn_4 nanowires, the deformation evolution of the single-crystalline Ni_3Sn_4 nanowire under uniaxial tensile stress can be majorly characterized by five major stages: bond straightening, bond breakage, inner atomic distortion, cross-section shrinking until forming a single-atom neck, and rupture.

(5) The Ni_3Sn_4 nanowire at a higher temperature is more inclined to undergo an early onset of atomic structure reconstruction; consequently, the yield strain and

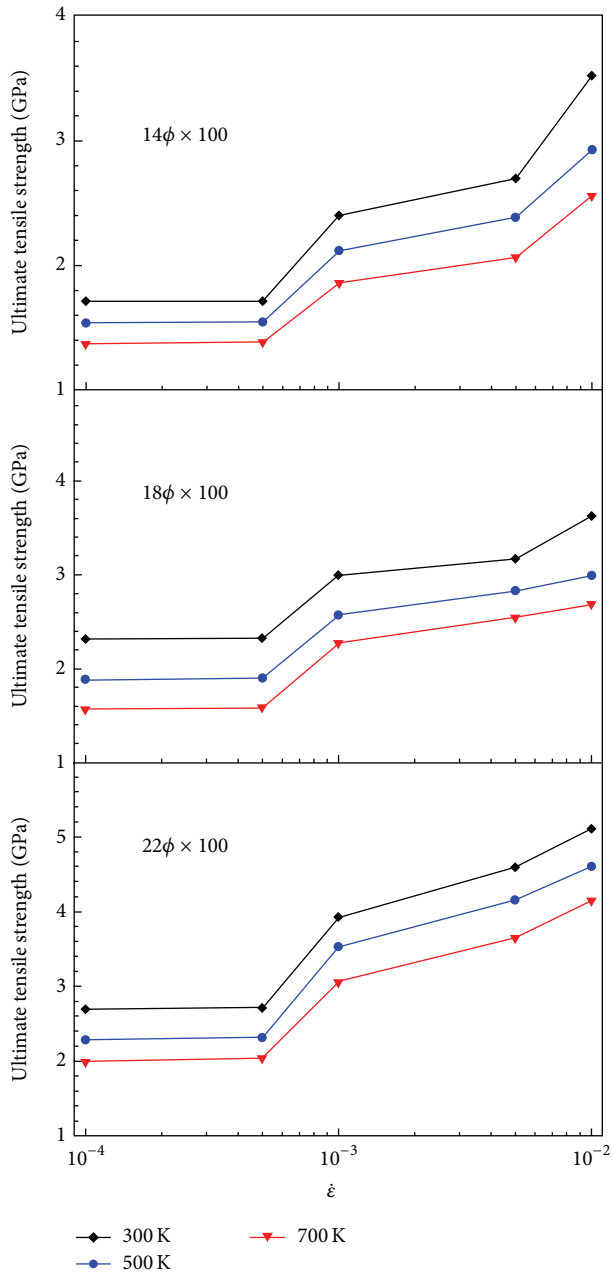

FIGURE 17: Effects of size, temperature, and strain rate on the ultimate tensile strength of the Ni_3Sn_4 nanowire models constructed along the x-axis.

strength and ultimate tensile strength and strain would all be considerably reduced.

(6) It is surprising to find that the Sn atoms in the Ni_3Sn_4 nanowire model tend to reside in the surface of the Ni_3Sn_4 nanowire while the Ni atoms would preferably stay inside the nanowire as the temperature increases from 300 K to 700 K, probably due to the larger cohesive energy in Ni atoms.

(7) The normal elastic constants are likely to be totally independent of the strain rate as the strain rate is below $5 \times 10^{-4}\%\ ps^{-1}$. Accordingly, the strain rate ($5 \times 10^{-4}\%\ ps^{-1}$) can be considered as the threshold value of the strain-rate dependence of the normal elastic constants of the Ni_3Sn_4 nanowire and the strain rates below which can be all treated as a quasistatic strain rate.

Conflict of Interests

The authors declare that there is no conflict of interests regarding the publication of this paper.

Acknowledgment

The work is partially supported by National Science Council, Taiwan, ROC, under Grants NSC101-2221-E-007-009-MY3 and NSC100-2221-E-035-036-MY3. The authors also thank the National Center for High-Performance Computing (NCHC) for computational resources support.

References

[1] T. W. Kim, K. L. Suk, S. H. Lee, and W. Paik, "Low temperature flex-on-flex assembly using polyvinylidene fluoride nanofiber incorporated sn58bi solder anisotropic conductive films and vertical ultrasonic bonding," *Journal of Nanomaterials*, vol. 2013, Article ID 534709, 10 pages, 2013.

[2] W. Zhang, B. Zhao, C. Zou, Q. Zhai, Y. Gao, and S. F. A. Acquah, "Investigating the formation process of Sn-based lead-free nanoparticles with a chemical reduction method," *Journal of Nanomaterials*, vol. 2013, Article ID 193725, 9 pages, 2013.

[3] F. E. Atalay, D. Avsar, H. Kaya, V. Yagmur, S. Atalay, and T. Seckin, "Nanowires of lead-free solder alloy SnCuAg," *Journal of Nanomaterials*, vol. 2011, Article ID 919853, 6 pages, 2011.

[4] H. C. Cheng, C. F. Yu, and W. H. Chen, "Strain- and strain-rate-dependent mechanical properties and behaviors of Cu_3Sn compound using molecular dynamics simulation," *Journal of Materials Science*, vol. 47, no. 7, pp. 3103–3114, 2012.

[5] B. D. Polat, N. Sezgin, O. Keles, K. Kazmanl, A. Abouimrane, and K. Amine, "A nano-architectured porous electrode assembly of copper richCu_6Sn_5 film for rechargeable lithium batteries," *Journal of Materials Science*, vol. 582, pp. 688–695, 2013.

[6] S. A. Belyakov and C. M. Gourlay, "$NiSn_4$ formation during the solidification of Sn-Ni alloys," *Intermetallics*, vol. 25, pp. 48–59, 2012.

[7] W. H. Chen, C. F. Yu, H. C. Cheng, Y. M. Tsai, and S. T. Lu, "IMC growth reaction and its effects on solder joint thermal cycling reliability of 3D chip stacking packaging," *Microelectronics Reliability*, vol. 53, no. 1, pp. 30–40, 2013.

[8] Y. C. Chan, P. L. Tu, C. W. Tang, K. C. Hung, and J. K. L. Lai, "Reliability studies of μBGA solder joints-effect of Ni-Sn intermetallic compound," *IEEE Transactions on Advanced Packaging*, vol. 24, no. 1, pp. 25–32, 2001.

[9] D. Yao and J. K. Shang, "Effect of aging on fatigue crack growth at sn-pb/cu interfaces," *Metallurgical and Materials Transactions A*, vol. 26, no. 10, pp. 2677–2685, 1995.

[10] J. Y. Kim, Y. C. Sohn, and J. Yu, "Effect of Cu content on the mechanical reliability of Ni/Sn-3.5Ag system," *Journal of Materials Research*, vol. 22, no. 3, pp. 770–776, 2007.

[11] L. C. Shen, C. W. Chien, H. C. Cheng, and C. T. Lin, "Development of three-dimensional chip stacking technology using a clamped through-silicon via interconnection," *Microelectronics Reliability*, vol. 50, no. 4, pp. 489–497, 2010.

[12] K. N. Tu, "Reliability challenges in 3D IC packaging technology," *Microelectronics Reliability*, vol. 51, no. 3, pp. 517–523, 2011.

[13] E. J. Cheng and Y.-L. Shen, "Thermal expansion behavior of through-silicon-via structures in three-dimensional microelectronic packaging," *Microelectronics Reliability*, vol. 52, no. 3, pp. 534–540, 2012.

[14] H. J. Albrecht, A. Juritza, K. Müller et al., "Interface reactions in microelectronic solder joints and associated intermetallic compounds: an investigation of their mechanical properties using nanoindentation," in *Proceedings of the IEEE Electronic Packaging Technology Conference*, pp. 726–731, Singapore, 2003.

[15] G. Gosh, "Elastic properties, hardness, and indentation fracture toughness of intermetallics relevant to electronic packaging," *Journal of Materials Research*, vol. 19, no. 5, pp. 1439–1454, 2004.

[16] X. Y. Pang, S. Q. Wang, L. Zhang, Z. Q. Liu, and J. K. Shang, "First principles calculation of elastic and lattice constants of orthorhombic Cu_3Sn crystal," *Journal of Alloys and Compounds*, vol. 466, no. 1-2, pp. 517–520, 2008.

[17] W. Zhou, L. Liu, and P. Wu, "Structural, electronic and thermoelastic properties of Cu_6Sn_5 and Cu_5Zn_8 intermetallic compounds: first-principles investigation," *Intermetallics*, vol. 18, pp. 922–928, 2010.

[18] W. H. Chen, C. F. Yu, H. C. Cheng, and S. T. Lu, "Crystal size and direction dependence of the elastic properties of Cu_3 Sn through molecular dynamics simulation and nanoindentation testing," *Microelectronics Reliability*, vol. 52, no. 8, pp. 1699–1710, 2012.

[19] H.-C. Cheng, C.-F. Yu, and W.-H. Chen, "First-principles density functional calculation of mechanical, thermodynamic and electronic properties of CuIn and Cu_2In crystals," *Journal of Alloys and Compounds*, vol. 546, pp. 286–295, 2012.

[20] H. C. Cheng, Y. L. Liu, Y. C. Hsu, and W. H. Chen, "Atomistic-continuum modeling for mechanical properties of single-walled carbon nanotubes," *International Journal of Solids and Structures*, vol. 46, no. 7-8, pp. 1695–1704, 2009.

[21] W. Chen, H. Cheng, and Y. Liu, "Radial mechanical properties of single-walled carbon nanotubes using modified molecular structure mechanics," *Computational Materials Science*, vol. 47, no. 4, pp. 985–993, 2010.

[22] Y. C. Shih, C. S. Chen, and K. C. Wu, "Chain length effect on surface stress of alkanethiolates adsorbed onto Au (111) surface: a van der waals density functional study," *Journal of Mechanics*, vol. 30, pp. 241–246, 2014.

[23] X. Y. You, L. D. Zhang, and J. R. Zheng, "The stability of finite miscible liquid-liquid stratified microchannel flow with boundary slip," *Journal of Mechanics*, vol. 30, no. 1, pp. 103–111, 2014.

[24] W. Chen, C. Wu, Y. Liu, and H. Cheng, "A theoretical investigation of thermal effects on vibrational behaviors of single-walled carbon nanotubes," *Computational Materials Science*, vol. 53, no. 1, pp. 226–233, 2012.

[25] J. Huang and D. Rodrigue, "Equivalent continuum models of carbon nanotube reinforced polypropylene composites," *Materials and Design*, vol. 50, pp. 936–945, 2013.

[26] W. H. Chen, H. C. Cheng, and Y. C. Hsu, "Mechanical properties of carbon nanotubes using molecular dynamics simulations with the inlayer van der Waals interactions," *CMES—Computer Modeling in Engineering and Sciences*, vol. 20, no. 2, pp. 123–145, 2007.

[27] W. H. Chen, H. C. Cheng, Y. C. Hsu, R. H. Uang, and J. S. Hsu, "Mechanical material characterization of Co nanowires and their nanocomposite," *Composites Science and Technology*, vol. 68, no. 15-16, pp. 3388–3395, 2008.

[28] H. C. Cheng, Y. C. Hsu, and W. H. Chen, "The influence of structural defect on mechanical properties and fracture behaviors of carbon nanotubes," *Computers, Materials and Continua*, vol. 11, no. 2, pp. 127–146, 2009.

[29] C. H. Wong and V. Vijayaraghavan, "Nanomechanics of non-ideal single- and double-walled carbon nanotubes," *Journal of Nanomaterials*, vol. 2012, Article ID 490872, 9 pages, 2012.

[30] H. Yu, C. Sun, W. W. Zhang, S. Y. Lei, and Q. A. Huang, "Study on size-dependent young's modulus of a silicon nanobeam by molecular dynamics simulation," *Journal of Nanomaterials*, vol. 2013, Article ID 319302, 5 pages, 2013.

[31] Z. Wan, J. D. Li, M. Jia, and J. L. Li, "Structural health monitoring (SHM) of three-dimensional braided composite material using carbon nanotube thread sensors," *Journal of Mechanics*, vol. 29, pp. 617–621, 2013.

[32] C. F. Yu, W. H. Chen, K. L. Chen, and H. C. Cheng, "Thermal-mechanical and thermodynamic properties of graphene sheets using a modified Nosé-Hoover thermostat," *Computers, Materials, and Continua*, vol. 36, no. 2, pp. 203–229, 2013.

[33] L. Meng, C. Yam, S. Koo, Q. Chen, N. Wong, and G. Chen, "Dynamic multiscale quantum mechanics/electromagnetics simulation method," *Journal of Chemical Theory and Computation*, vol. 8, no. 4, pp. 1190–1199, 2012.

[34] J. Jeon and M. Cho, "Direct quantum mechanical/molecular mechanical simulations of two-dimensional vibrational responses: N-methylacetamide in water," *New Journal of Physics*, vol. 12, Article ID 065001, 2010.

[35] H. C. Cheng, C. F. Yu, and W. H. Chen, "Physical, mechanical, thermodynamic and electronic characterization of $Cu_{11}In_9$ crystal using first-principles density functional theory calculation," *Computational Materials Science*, vol. 81, pp. 146–157, 2014.

[36] N. T. S. Lee, V. B. C. Tan, and K. M. Lim, "Structural and mechanical properties of Sn-based intermetallics from initio-calculations," *Applied Physics Letters*, vol. 89, Article ID 141908, 2006.

[37] F. Gao and J. Qu, "Elastic moduli of $(Ni, Cu)_3Sn_4$ alloys from first-principles calculations," *Journal of Electronic Materials*, vol. 39, pp. 2429–2434, 2010.

[38] M. C. Payne, M. P. Teter, D. C. Allan, T. A. Arias, and J. D. Joannopoulos, "Iterative minimization techniques for ab initio total-energy calculations: molecular dynamics and conjugate gradients," *Reviews of Modern Physics*, vol. 64, no. 4, pp. 1045–1097, 1992.

[39] L. Dong and S. P. Alpay, "Polarization, piezoelectric properties, and elastic coefficients of in_x Ga_{1-x} N solid solutions from first principles," *Journal of Materials Science*, vol. 47, no. 21, pp. 7587–7593, 2012.

[40] C. J. Casewit, K. S. Colwell, and A. K. Rappé, "Application of a universal force field to main group compounds," *Journal of the American Chemical Society*, vol. 114, no. 25, pp. 10046–10053, 1992.

[41] A. K. Rappé, K. S. Colwell, and C. J. Casewit, "Application of a universal force field to metal complexes," *Inorganic Chemistry*, vol. 32, no. 16, pp. 3438–3450, 1993.

[42] W. Jeitschko and B. Jaberg, "Structure refinement of Ni_3Sn_4," *Acta Crystallographica B*, vol. 38, pp. 598–600, 1982.

[43] B. L. Wang, S. Y. Yin, G. H. Wang, A. Buldum, and J. Zhao, "Novel structures and properties of gold nanowires," *Physical Review Letters*, vol. 86, no. 10, pp. 2046–2049, 2001.

[44] J. Diao, K. Gall, and M. L. Dunn, "Surface-stress-induced phase transformation in metal nanowires," *Nature Materials*, vol. 2, no. 10, pp. 656–660, 2003.

[45] O. Gülseren, F. Ercolessi, and E. Tosatti, "Premelting of thin wires," *Physical Review B*, vol. 51, no. 11, pp. 7377–7380, 1995.

[46] H. J. C. Berendsen, J. P. M. Postma, W. F. Van Gunsteren, A. Dinola, and J. R. Haak, "Molecular dynamics with coupling to an external bath," *The Journal of Chemical Physics*, vol. 81, no. 8, pp. 3684–3690, 1984.

[47] C. C. Lee, P. J. Wang, and J. S. Kim, "Are intermetallics in solder joints really brittle?" in *Proceedings of the 57th Electronic Components and Technology Conference (ECTC '07)*, pp. 648–652, Reno, NV, USA, June 2007.

[48] M. Zhou, "A new look at the atomic level virial stress: on continuum-molecular system equivalence," *Proceedings of the Royal Society A: Mathematical, Physical and Engineering Sciences*, vol. 459, no. 2037, pp. 2347–2392, 2003.

[49] H. Ikeda, Y. Qi, T. Çağin, K. Samwer, W. L. Johnson, and W. A. Goddard, "Strain rate induced amorphisation in metallic nanowires," *Physical Review Letters*, vol. 82, pp. 2900–2903, 1999.

[50] S. J. A. Koh, H. P. Lee, C. Lu, and Q. H. Cheng, "Molecular dynamics simulation of a solid platinum nanowire under uniaxial tensile strain: Temperature and strain-rate effects," *Physical Review B: Condensed Matter and Materials Physics*, vol. 72, no. 8, Article ID 085414, 2005.

[51] Y. Gan and J. K. Chen, "Molecular dynamics study of size, temperature and strain rate effects on mechanical properties of gold nanofilms," *Applied Physics A: Materials Science & Processing*, vol. 95, no. 2, pp. 357–362, 2009.

[52] H. A. Wu, "Molecular dynamics study on mechanics of metal nanowire," *Mechanics Research Communications*, vol. 33, pp. 9–16, 2006.

[53] R. Dingreville, J. Qu, and M. Cherkaoui, "Surface free energy and its effect on the elastic behavior of nano-sized particles, wires and films," *Journal of the Mechanics and Physics of Solids*, vol. 53, no. 8, pp. 1827–1854, 2005.

[54] R. C. Cammarata and K. Sieradzki, "Effects of surface stress on the elastic moduli of thin films and superlattices," *Physical Review Letters*, vol. 62, no. 17, pp. 2005–2008, 1989.

[55] J. G. Guo and Y. P. Zhao, "The size-dependent elastic properties of nanofilms with surface effects," *Journal Applied Physics*, vol. 98, Article ID 074306, 2005.

[56] C. Kittel, *Introduction to Solid State Physics*, John Wiley & Sons, Hoboken, NJ, USA, 8th edition, 2005.

[57] P. S. Branício and J.-P. Rino, "Large deformation and amorphization of Ni nanowires under uniaxial strain: a molecular dynamics study," *Physical Review B: Condensed Matter and Materials Physics*, vol. 62, no. 24, pp. 16950–16955, 2000.

[58] S. K. R. S. Sankaranarayanan, V. R. Bhethanabotla, and B. Joseph, "Molecular dynamics simulation of temperature and strain rate effects on the elastic properties of bimetallic Pd-Pt nanowires," *Physical Review B*, vol. 76, no. 13, Article ID 134117, 2007.